Dieses Dokument ist eine Zweitveröffentlichung (Verlagsversion) /

This is a self-archiving document (published version):

SLUB
Wir führen Wissen.

TECHNISCHE
UNIVERSITÄT
DRESDEN

QUCOSA
Quality Content of Saxony

AFM-based mechanical characterization of single nanofibres

Benedikt R. Neugirg,†[a] Sean R. Koebley,†[b] Hannes C. Schniepp*[b] and Andreas Fery*[c,d]

Nanofibres are found in a broad variety of hierarchical biological systems as fundamental structural units, and nanofibrillar components are playing an increasing role in the development of advanced functional materials. Accurate determination of the mechanical properties of single nanofibres is thus of great interest, yet measurement of these properties is challenging due to the intricate specimen handling and the exceptional force and deformation resolution that is required. The atomic force microscope (AFM) has emerged as an effective, reliable tool in the investigation of nanofibrillar mechanics, with the three most popular approaches—AFM-based tensile testing, three-point deformation testing, and nanoindentation—proving preferable to conventional tensile testing in many (but not all) cases. Here, we review the capabilities and limitations of each of these methods and give a comprehensive overview of the recent advances in this field.

Introduction

Fibres of nanoscale diameter form the fundamental building blocks of numerous mechanically superior natural and synthetic materials, yet precise determination of the mechanical

[a]*Department of Physical Chemistry II, University of Bayreuth, Bayreuth 95440, Germany*
[b]*Department of Applied Science, The College of William & Mary, Williamsburg, VA 23187, USA. E-mail: schniepp@wm.edu*
[c]*Leibniz-Institut für Polymerforschung Dresden e. V., Institute of Physical Chemistry and Polymer Physics, Dresden 01069, Germany. E-mail: fery@ipfdd.de*
[d]*Chair for Physical Chemistry of Polymeric Materials, Technical University Dresden, Dresden 01069, Germany*
†These authors contributed equally to this work.

properties of these fibres remains challenging. Wood, bone,[1] and carbon fibre composites[2] are just a few examples of natural and synthetic materials with extreme strength-to-weight ratios that share a common hierarchical design: robust nanofibres embedded in a supporting matrix. Beyond the mechanical stability in composites, many manufactured quasi one-dimensional objects of nanoscale diameter (*i.e.* fibres, wires, tubes, whiskers, *etc.*, collectively termed "fibres" in this review) combine different distinct functionalities that render them specifically interesting from an applications perspective.[3–6] The nanoscale diameters are believed to both decrease the probability of flaws or defects and increase the fibre's surface area-to-volume ratio, hence causing physical properties distinct from bulk.[3,5–8] Advanced synthetic[9] and

Benedikt R. Neugirg is a PhD student in the graduate school (BayNAT) at the University of Bayreuth, Germany under the supervision of Prof. Andreas Fery. He received his BSc in chemistry in 2010 and his MSc in material chemistry and catalysis in 2012 from the University of Bayreuth, Germany. His research focuses on the characterization of fibrillar systems via atomic force microscopy.

Benedikt R. Neugirg

Sean R. Koebley earned a Bachelor of Science in Biology and Minor in Mathematics from The College of William & Mary in 2008. He taught middle school mathematics in Boston and Washington, D.C. before returning to William & Mary in 2011 to pursue a PhD in Applied Science with a concentration in Materials Science & Engineering. Under the supervision of Hannes Schniepp, he uses atomic force microscopy and other techniques to study the structure, mechanical properties, and assembly of silk.

Sean R. Koebley

preparation approaches[10] to produce such high aspect ratio fibres pave the way for widespread potential applications; for instance, implementation of metallic nanowires or carbon nanotubes in electrical devices,[2,9] tough and biocompatible artificial spider silk fibres,[11] and electrospun polymer fibres for tissue engineering[12] or functional scaffolds.[13]

Characterizing and understanding the fibres' mechanical properties are important in each of these implementations. However, most conventional testing techniques fail when fibre diameters and lengths undercut approximately one micron and several mm, respectively. The force sensing capabilities and spatial resolution of the atomic force microscope (AFM) allow one to overcome these challenges, and several AFM-based mechanical nanofibre testing approaches have emerged. Here, we review the most common of these approaches: AFM-based tensile testing, three-point deformation testing, and quasi-static nanoindentation (Fig. 1).

AFM-based tensile testing

The standard technique for acquiring a fibre's mechanical properties is tensile testing, which involves extending the fibre ends in opposite directions at a controlled rate while monitoring the force using a capacitor load cell. This method is well-established, accurate, and involves a simple attachment of the fibre ends *via* clamping. However, conventional tensile testing is not applicable in many nanoscale systems. The tensile tester most specialized for the characterization of nanofibres has a claimed force sensitivity of 50 nN and extension resolution of 35 nm.[15,16] For a rough estimate of the thinnest, weakest fibre that can be tested with the claimed 50 nN sensitivity, we assume that at least 100 discrete force delineations in the resulting stress–strain curve are desired. With this requirement, tested fibres must approximately satisfy 5 μN < $A\sigma_u$ =

$\pi(D/2)^2\sigma_u$, where σ_u is the fibre's ultimate strength, A is the cross-sectional area, and D is the cylindrical fibre diameter. The mechanical properties of a fibre can therefore be probed with a tensile tester if $D > \sqrt{\dfrac{20\ \mu N}{\pi\sigma_u}}$. Another, potentially more serious challenge to nanoscale tensile testing is sample preparation, which demands that the fibre be suspended between the two arms of the tensile tester. The fibre must therefore be at least ≈1 mm in length (5 mm is typical) and freestanding—conditions that are often attainable by microscale fibres such as spider silks,[17–19] but only rarely met by nanoscale fibres, *e.g.* in some studies of electrospun polymers.[20–24]

AFM-based tensile testing is a similar approach to conventional tensile testing that is in principle not limited by fibre length or force sensitivity, yet employs the same deformation geometry of uniaxial stretching along the fibre axis. In this method, which is a form of force spectroscopy, a nanofibrillar sample—*e.g.* carbon nanotube,[25] WS$_2$ nanotube,[26] gold nanowire,[27,28] polymer fibre,[29–31] or collagen fibril[29,32–36]—is grown or attached to both the AFM probe tip and the substrate, and the force on the tip is determined as the probe is retracted. Similarly, material can be attached to an AFM tip, manipulated into a fibrillar, dogbone-shaped structure using a focused ion beam (FIB), and force spectroscopy can be conducted to yield the material's stress–strain response.[37] The force and spatial resolution of the AFM surpasses that of even the most sensitive tensile tester by approximately two orders of magnitude, as the loading force in an AFM is applied by piezoelectric actuators to a microscopic cantilever and the resulting force is usually measured by reflecting a laser off the cantilever's backside and onto a photodiode.[38] The long optical path of the laser in this setup allows for the detection of minute cantilever deflections, resulting in pN force sensitivity for suitable cantilevers. A thorough calibration of the cantilever as the central force sensing element is crucial, and typically involves: (a) measure-

Hannes Schniepp earned a Diploma in Physics at the University of Konstanz (Germany) in 1999 under the supervision of Jürgen Mlynek, and received his PhD in Chemistry and Applied Biosciences at the Swiss Federal Institute of Technology (ETH Zürich) in 2004 under the supervision of Vahid Sandoghdar. From there, he joined Ilhan Aksay's group in the chemical engineering department at Princeton University as a postdoctoral researcher. Since 2008 he has been a faculty member at the College of William & Mary, currently as the Adina Allen Term Distinguished Associate Professor of Applied Science. The research of his group is focused on nano- and biomaterials.

Hannes C. Schniepp

Andreas Fery studied Physics and did his PhD at the Max-Planck Institute for Colloids and Interfaces (MPIKG)/Potsdam University in 2000. After a post-doc at Institute Curie, he became group leader at MPIKG. In 2007 he joined Bayreuth University as professor. Since 2015 he is head of the institute for Physical Chemistry/Polymer Physics at the Leibniz Institut für Polymerforschung Dresden. He received the Richard Zsigmondy award of the German colloid society and an ERC starting grant. He has published >180 papers in the area of Polymer science and Colloid- and interface science, which have received >4000 citations.
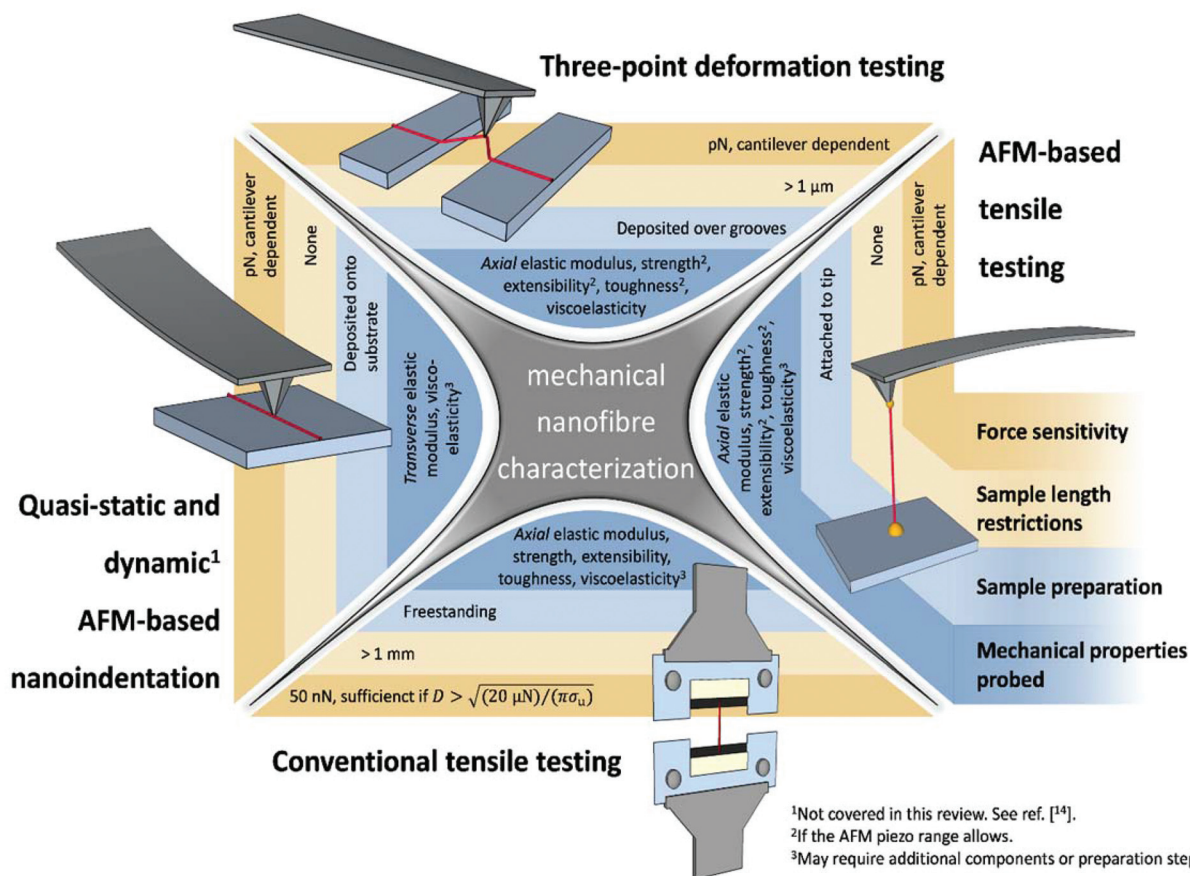
Andreas Fery

Fig. 1 Schematic overview of the major conventional and AFM-based techniques for measuring the mechanical properties of nanofibres. Each technique is characterized by its force sensitivity, restrictions on the sample length, sample preparation requirements, and mechanical properties probed. See ref. 14 for a review of dynamic nanoindentation.

ment of the inverse optical lever sensitivity (InvOLS) $[m\ V^{-1}]$,[39] which relates the photo voltage signal to the cantilever deflection, and (b) obtaining the cantilever's spring constant $[N\ m^{-1}]$,[40–42] which allows conversion of cantilever deflection into force F. To yield d—the probe tip's true distance from the surface or, if the tip and sample are in contact, the deformation of the sample—it is necessary to subtract the cantilever's deflection from the raw z-displacement data.[38] Notably, the cantilever spring constant in an AFM-based nanomechanical experiment must closely match the effective sample spring constant in order to achieve the appropriate force sensitivity; otherwise, deflection may either exceed the range of the photodiode (if the cantilever is too soft) or be so weak as to be indistinguishable from systemic noise (if the cantilever is too stiff).[43,44]

Nanoscale tensile testing conducted both with the AFM and with specialized microelectromechanical systems (MEMS)[45–51] has produced reliable results for nanofibres. However, attachment of the fibre in these arrangements is tedious and may be prohibitive in many cases: the fibre must be grown between tip and sample[27,28] or attached *via* elaborate micromanipulation[30–32,34–36] that often requires the use of a combination SEM–AFM system.[25,26,29,33,37] If imaging and treatment in an SEM is involved, the sample usually becomes

dehydrated, and in some cases metallic coatings are applied to the sample to provide electrical conductivity, which may further alter its mechanical properties. Similarly, ion bombardment in a FIB must be executed with particular caution, as it has been shown to mechanically strengthen the sample.[52,53] In light of these preparation complexities, alternative techniques with fewer sample manipulation and attachment demands are often desirable.

AFM-based three-point deformation testing

Overview

In most AFM-based three-point deformation tests, sample preparation is as simple as depositing fibres onto a hard substrate that is prestructured with grooves. Fibres will statistically span these grooves, leaving segments suspended. The suspended portions of the fibres can then be probed by an AFM cantilever tip to perform a three-point deformation test. This approach achieves nanoscale force and spatial resolution, allowing for specimens with nanometer-sized diameters and lengths below 1 μm, *e.g.* individual single-walled carbon nano-

tubes.[54] In most cases, the three-point deformation test primarily aims to determine the axial Young's modulus of fibres, the modulus also probed by tensile testing. By adjusting the suspended length and deformation range, one can further determine the bending and shear moduli,[55] yield point,[56] viscoelasticity,[57] toughness and strength,[58] and even rupture properties such as a fibre's extensibility.[59] Beyond probing mechanical parameters under standard conditions, the AFM's general tolerance for different ambient conditions enables a widespread range of samples and facilitates testing of the fibres' performance in different media[60,61] or at different temperatures,[62] as well as their *in situ* responsiveness to pH changes.[63] Furthermore, the testing setup can be combined with conductivity measurements to directly monitor the strain dependence of current flow across the fibre.[54,64,65]

Experimentally, three-point deformation tests can be distinguished by their loading direction relative to the substrate and

deformation range: the test involves either vertical loading and a relatively small deformation (Fig. 2a) or lateral loading and a large deformation (Fig. 2b). In the former approach, the cantilever moves vertically (in the *z*-direction), pressing the suspended fibre segment downwards while being deflected upwards. For vertical cantilever deflections, calibration is more straightforward; however, the limited displacement of the *z*-piezo (typically ≈10 μm) confines the range of fibre deformation. Hence, vertical three-point bending is sometimes limited to small deflections of relaxed fibres in the linear elastic regime, and is thus ideally suited to determining the fibre's axial Young's modulus or its bending and shear moduli.[55,60,68]

In the second approach – lateral loading – the cantilever tip travels in the *x,y*-plane and intersects the suspended fibre segment perpendicularly at its midpoint (Fig. 2b). The fibre experiences both bending and stretching, imposing torsion on
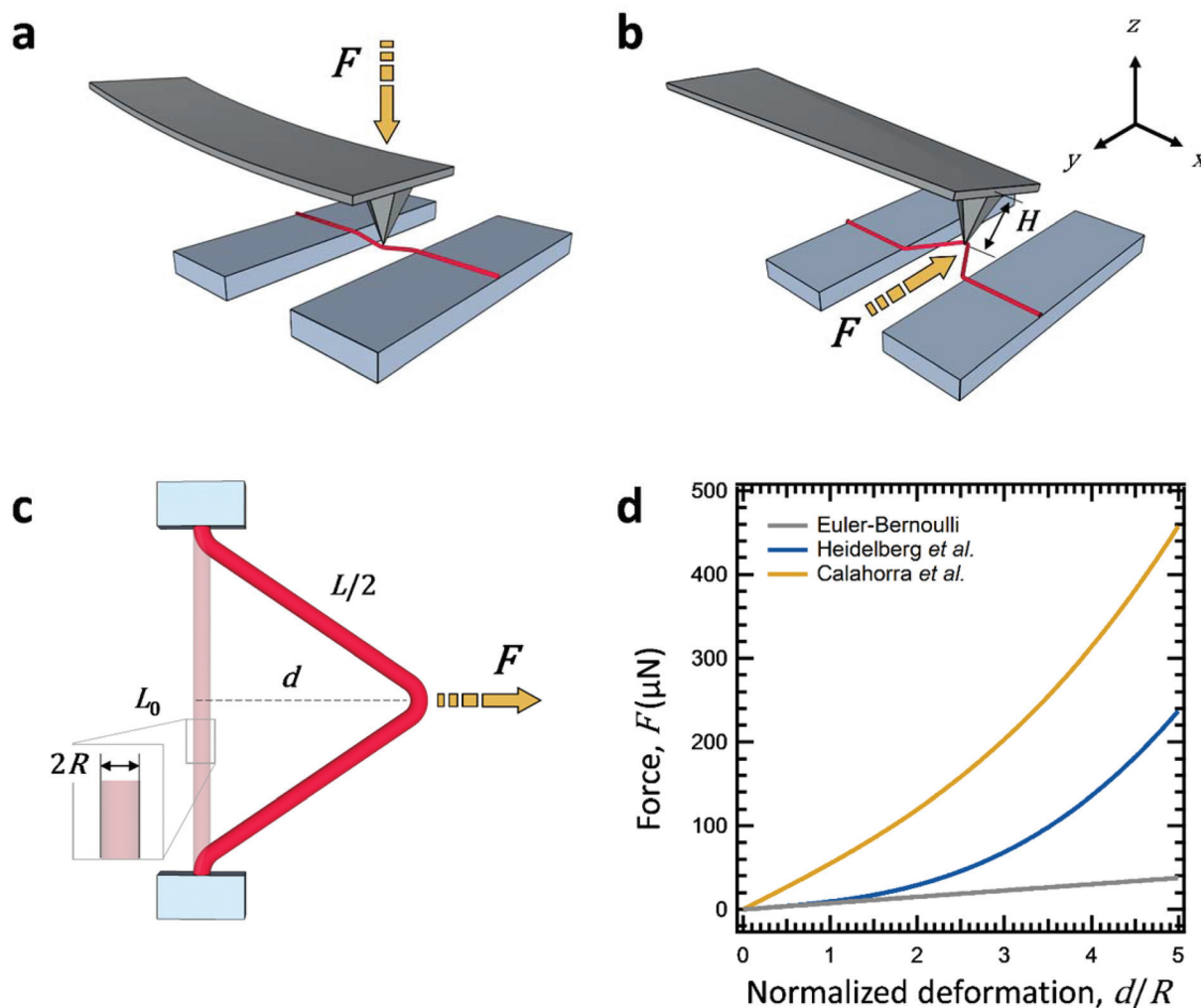

Fig. 2 Schematics of vertical (a) and lateral (b) three-point deformation testing. In both approaches a (usually clamped) fibre segment is subjected to a load. Denominations of the physical values are given in (c). Exemplary force *vs.* deformation (normalized to the fibre radius) dependencies according to the models of Euler–Bernoulli (pure bending), Heidelberg *et al.*[66] (bending and stretching), and Calahorra *et al.*[67] (bending and stretching of a pre-strained fibre) are given in (d).

the cantilever at a certain lever arm H (Fig. 2b), which is defined as the distance from the cantilever long axis to the tip's contact point with the fibre. This torsion renders the data conversion to forces more intricate, as the lateral optical lever sensitivity and the lateral spring constant need to be known precisely. To date, no experimental method to obtain these two parameters has emerged as general standard, yet, various approaches exist: the lateral spring constant for instance can be derived using the torsional Sader method[69] or by calculation from cantilever dimensions. The reader is referred to a recent comprehensive review on this topic by Munz.[70] Nevertheless, exploiting the generally larger x,y-piezo reach by lateral loading facilitates larger fibre deformations, enabling a complete mechanical characterization—from the elastic regime to rupture.

Pure bending regime

Regardless of loading direction, both testing techniques deform the fibre perpendicular to its long axis, causing similar strains in a radially symmetric specimen. Deformations of less than one fibre radius predominantly cause bending: at the bending points (the edges of the grooves and the tip–fibre contact), the convex side experiences tensile strain, while the concave side experiences compressive strain. Additionally, these strains increase radially from the neutral plane to the fibre surface, resulting in an inhomogeneous stress distribution with local stress peaks. These bending deformations can be well described by the classical Euler–Bernoulli beam model, which takes into account the fibre's boundary conditions, i.e. whether it is simply supported by or firmly attached to the substrate.[71]

An advantage of the vertical loading approach is the relative ease of using force–volume plots[61,68,72–74] or advanced force imaging techniques,[75,76] which allow one to map the fibre response as a function of position and thereby directly determine the present boundary conditions. If F is the force applied at the position x along the fibre axis, causing a deformation d, the ratio of $F(x)/d$ can be interpreted as the fibre's stiffness at the respective position (Fig. 2c). A measured stiffness profile along the suspended segment can then be compared to models for different boundary conditions. For a simply supported beam, the model suggests:

$$\frac{F(x)}{d} = \frac{3L_0 EI}{(L_0 - x)^2 x^2} \tag{1}$$

In the case of a double-clamped beam one finds:

$$\frac{F(x)}{d} = \frac{3L_0{}^3 EI}{(L_0 - x)^3 x^3} \tag{2}$$

In both cases, L_0 is the initial length of the suspended segment, E is the axial Young's modulus, and I is the area moment of inertia, where $I = \pi R^4/4$ for cylindrical fibres with radius R (Fig. 2c).

Kluge et al. compared the rigidities and Young's moduli derived from such stiffness profiles of three different 1,3,5-benzenetrisamides that each self-assemble into supramolecular nanofibres.[68] They focused on results where the boundary conditions were unambiguously found to be double-clamped and measured Young's moduli in the lower GPa range. In contrast, Ling et al. found self-supporting particle bridges cohered by a supramolecular glue to follow the model of a simply supported beam.[77] This shows that clamping of the fibre to the supports is not absolutely necessary as long as clamping conditions are determined in each situation, especially since data interpretation in the framework of the wrong boundary conditions would lead to a Young's modulus off by a factor of 4 (as approximated using $x = L_0/2$ and comparing eqn (1) and (2)). In other studies, both boundary conditions and, occasionally, a mixed case (one side clamped, one simply supported) were observed within one respective fibre–substrate system.[74,75,78] For instance, Chen et al. probed the stiffness profiles of silver nanowires with diameters between 66 and 141 nm using digital pulsed force mode.[75] They pointed out the importance of the boundary conditions, as thinner nanowires resembled a double clamped beam whereas thicker ones were simply supported. Both cases yielded moduli close to the bulk value of silver.

In the majority of three-point bending studies, however, fibres are assumed to be double clamped due to sufficient fibre–substrate adhesion[79,80] or double clamped conditions are enforced by additional experimental measures.[56,81] Probing with a force F_c at the segment midpoint ($x = L_0/2$) reduces eqn (2) to:

$$F(L_0/2) = F_c = \frac{192EI}{L_0{}^3} \cdot d \tag{3}$$

(gray line, Fig. 2d). Due to the shape of the stiffness profile (eqn (2)), the force response is relatively insensitive to small positioning deviations from the midpoint, increasing the robustness of the method.[82,83] In the case of sufficient fibre–substrate adhesion, the midpoint probing approach allows for relatively low expenditure of experimental time, hence facilitating larger sample numbers. For example, Stachewicz et al. provided a thorough experimental basis demonstrating a modulus increase with decreasing diameter for electrospun polyvinyl-alcohol fibres.[80] They attributed this trend to the fibres' core–shell structure caused by the high shear in electrospinning.

The superposition of bending and stretching

Lateral three-point deformation tests mostly deform fibres beyond the bending regime (deformation d exceeding the fibre radius R), and often aim to break or rupture the fibre. As the fibre is increasingly stretched, tensile stresses in the straight specimen portions are superimposed with tensile and compressive stresses at the bending points (as mentioned above). For large yet elastic deformations, Heidelberg et al. introduced a factor $f(\alpha) > 1$ to account for this resulting rigidity enhancement in double clamped beams (blue line, Fig. 2d).[66]

$$F_c = \frac{192EI}{L_0{}^3} \cdot f(\alpha) \cdot d \tag{4}$$

where

$$f(\alpha) = \frac{\alpha}{48 - \dfrac{192 \tan h(\sqrt{\alpha}/4)}{\sqrt{\alpha}}}, \tag{5}$$

$$\alpha = \frac{6\varepsilon(140 + \varepsilon)}{350 + 3\varepsilon} \tag{6}$$

and

$$\varepsilon = d^2(A/I) \tag{7}$$

Here, A is the fibre's cross-sectional area. This model succeeds in describing the full elastic response of a fibre, e.g. high-modulus inorganic nanowires,[64,66,84–87] therefore allowing the transition from elastic to plastic deformation to be determined. Wen et al. applied this model to demonstrate that the Young's modulus of ZnO nanowires resembles the bulk value and can be regarded essentially diameter-independent in the range from 18 to 304 nm.[86] Recently, McCarthy et al. used eqn (4)–(7) to calculate the Young's modulus of nickel and silver nanowires and to verify the elasticity of the applied deformations, a prerequisite for their determination of the Poisson's ratio of these wires from strain-dependent four-point resistance measurements.[64] Furthermore, since this model extends to higher deformations than classical bending (eqn (3)), it is more sensitive to experimental inconsistencies. For instance, pre-strained fibres can be identified since their deformation data would not fit the model, and modulus overestimation can hence be prevented (see Fig. 2d).

The role of pre-tension

Despite its applicability over the full elastic regime, the Heidelberg model was not employed for soft matter fibres at all, probably because of significant residual tension in these systems. With decreasing material modulus, pre-tension inherent in a fibre (from the preparation or clamping procedure) increasingly dominates its force response. This is manifested in a steeper slope of the initial linear bending regime (where $d < R$) in force–deformation curves (yellow line, Fig. 2d). Pre-tension was first investigated in spider mite silk, in which tension was naturally introduced as the mites drew silk from their spinning glands and deposited it onto the test substrate.[82] Hudson et al. implemented the effect of pre-tension in a numerical model by expanding the factor $f(\alpha)$ in eqn (4).[82] Calahorra et al., who also recently observed such residual stresses in hard silicon nanowires, approximated the full solution for the expanded $f(\alpha)$ by an analytical expression[67,88] for the ease of application:

$$f_{approx}(\alpha_{approx}) = 1 + 2.412 \times 10^{-2}\,\alpha_{approx} - 1.407 \\ \times 10^{-6}\,\alpha_{approx}^2 \tag{8}$$

where α_{approx} includes the initial pre-tension force T_0:

$$\alpha_{approx} = \frac{L_0^2 T_0}{EI} + \frac{6\varepsilon(140 + \varepsilon)}{350 + 3\varepsilon} \tag{9}$$

The Heidelberg model, now expanded for pre-tension, enables a comprehensive data interpretation of elastic deformations in double clamped three-point deformation tests. Beyond the limit of one fibre radius of deformation, the tensile contribution increasingly dominates the fibre's force response. In that regime, the linear dependence of force on deformation passes into a cubic dependence, rendering the bending contributions gradually negligible. In the work of Schniepp et al., thin ribbons of nanometer thickness were deformed several μm to derive the Young's modulus based on a purely tensile model, as the bending component is negligible for thin ribbons.[89] Presuming only stretching of the fibre, one can easily convert the measured force and deformation to (axial) stress and strain.[58,90] This approach yields lower estimates for fibre failure properties, such as maximum strength, extensibility and toughness.[54,57,58,89,90] Biopolymer fibres were mechanically characterized using this same approach, revealing the extraordinary extensibility of fibrin[59,91] and viscoelastic properties of collagen fibres.[92]

AFM nanoindentation

Overview

Another AFM-based technique can be applied to nanofibres that are simply deposited onto a flat substrate: nanoindentation (Fig. 3). Nanoindentation is an established technique that is traditionally performed by an instrumented nanoindenter, which is reliable in acquiring the elastic modulus of a wide range of materials, from hard surfaces, e.g. silicon,[93,94] to relatively soft polymer composites.[95] However, an instrumented nanoindenter's capacitor-based force sensor and the typically employed probes necessitate micron-scale contact areas and indentation depths, making it an unacceptable tool for nanoscale structures.[94,96] Similarly, an AFM-nanoindenter combination instrument—which employs a standard nanoindenter probe within a system with the positional sensitivity of an AFM and improved force sensitivity[97,98]—has been successfully implemented in studies of nanofibrils,[99–103] yet is limited by the larger size of its probe.

Due to its nanoscale probe tips, superb force sensitivity, and translational accuracy, the AFM has emerged in recent years as an ideal choice for performing nanoindentation on a variety of nanoscale structures.[104–106] Here, we consider AFM-based nanoindentation of nanoscale fibrils via static and quasi-static indentation—the simplest modes—in which the frequency of one complete indentation is far less than the resonance frequency of the cantilever, allowing for instantaneous response to force deviations.[43] However, many of the considerations discussed here also apply to dynamic nanoindentation techniques.[14]

Typical examples of quasi-static AFM force–indentation curves conducted on fibrillar samples are shown in Fig. 4. Following the standard InvOLS and cantilever spring constant calibrations, displacement-to-indentation calibration must be performed on a reference sample that is much stiffer than the
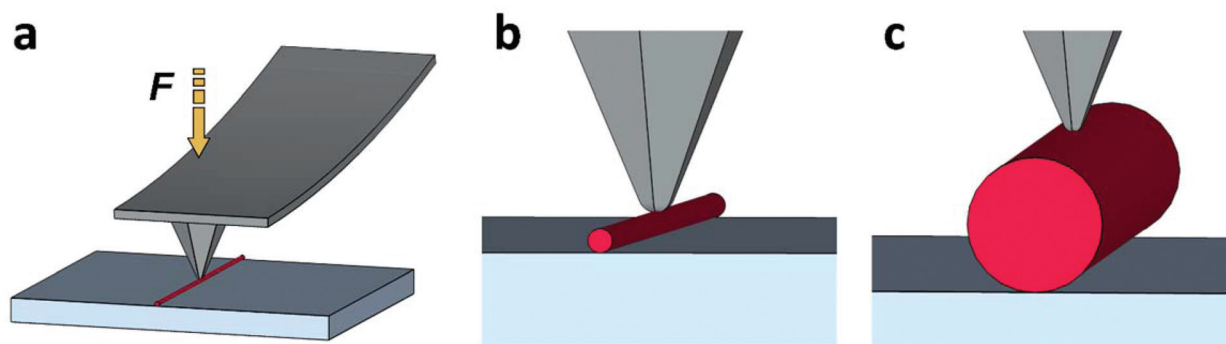
Fig. 3 (a) AFM nanoindentation of a fibril with force F, which can be conducted on samples where (b) the diameter of the AFM tip is about equal to or less than the diameter of the fibril ($D_{fib} \approx D_{tip}$ or $D_{fib} < D_{tip}$), or (c) the diameter of the tip is far less than the diameter of the fibril ($D_{fib} \gg D_{tip}$).

sample of interest. The resulting force–indentation curve of this reference sample (*e.g.* silica) is vertical at $d = 0$, reflecting the assumed lack of indentation into the stiff substrate at the forces involved (Fig. 4a, blue curve). When a force curve is then conducted on a much softer material (*e.g.* collagen), indentation takes place past $d = 0$ (Fig. 4a red curve, Fig. 4b). Hysteresis often occurs between the loading and unloading curves due to the plastic response of the sample: loading induces plastic deformation, and unloading reflects the elastic recovery of the material (Fig. 4b).[108] Thus, to derive the elastic modulus of the material, the unloading curve is typically chosen for fitting.

The slope of the unloading curve roughly corresponds to the transverse elastic modulus of the material—the modulus sampled when performing tests perpendicular to the fibre axis —but quantitative, reliable determination of the modulus requires fitting the appropriate contact model to the data. Four contact model choices are most widely used in indentation studies: Hertz, Derjaguin–Muller–Toporov (DMT), Johnson–Kendall–Roberts (JKR), and Oliver–Pharr. The starting point in contact mechanics, the Hertz model,[111] describes the purely elastic force response of two spheres indenting one another ("+" markers, Fig. 4a):

$$F = \frac{4}{3} \frac{\sqrt{R_{eff}}}{1-\nu^2} E_T d^{3/2} \qquad (10)$$

where ν is Poisson's ratio, $R_{eff} = (1/R_{tip} + 1/R_{fib})^{-1}$ is the effective radius of contact, and E_T is the fibril transverse elastic modulus. The DMT model is based on the Hertz model, but accounts for adhesion between the probe and sample.[112,113] To describe contact between a larger tip and a softer sample, in which larger adhesion forces are experienced, the JKR model is preferred.[112,113] The Oliver–Pharr model,[108,109] which has been considered the standard in traditional nanoindentation studies since 1992,[94] gives the force response of an arbitrarily shaped probe indenting an elastic-plastic flat surface but neglecting adhesion (Fig. 4b and c). The modulus is derived from the elastic unloading stiffness (S)—the slope of the upper portion of the unloading curve (Fig. 4b)—according to:

$$E_T = \beta \frac{\sqrt{\pi}}{2} (1-\nu^2) \frac{S}{\sqrt{A_i(d_c)}} \qquad (11)$$

where β is an empirical correction factor, d_c is the depth of contact between the indenter and sample, and A_i is the indenter-sample contact area (Fig. 4b and c).[108,109] $A_i(d_c)$ may be determined for a pyramidal, spherical, or arbitrarily shaped indenter[110] as long as the probe shape is known.[108]

Tip shape

To obtain quantitative results in AFM-based nanoindentation, a number of experimental factors must be addressed. First, in order to accurately describe the probe–sample contact area *vs.* probe indentation depth—a crucial aspect of any contact model—the volumetric tip profile must be precisely determined. Most often, a calibration sample of known topography (spikes or sharp edge) is scanned by the tip of interest to quickly obtain a putative profile, but the shape of the scanned test features must then be deconvoluted in order to obtain the most accurate tip shape.[110,114] An alternative to mapping a detailed profile of the tip is to test a reference sample of known modulus—a technique widely adopted and automated in quasi-static PeakForce QNM and other similar techniques.[43,115–117] However, the indentation depth must be kept consistent between the reference and test samples,[118] and the reference sample should ideally reflect the geometry of the test sample if the same indentation model is to be applied to each.[103] Thus, tests of samples like cylindrical fibrils that depart from the semi-infinite plane geometry of the standard reference sample may be subject to unanticipated inaccuracy.

Indentation location

An attractive feature of nanoindentation is its ease of sample preparation: fibrils can be dispersed on any substrate and tested in air or aqueous solution. To ensure that the indentation is conducted on a fibril, the simultaneous collection of topography and modulus data is preferred,[107,110,119] and may be achieved by a quasi-static technique like force–volume mapping.[120] Only indentations along the fibril's spine should be used in modulus calculations.[107,110,119] If the side of a fibril is indented instead, the contact area becomes highly unpredictable or unaccounted-for in the employed model.[110,119] Lateral deflection is also likely to occur in such a case, further
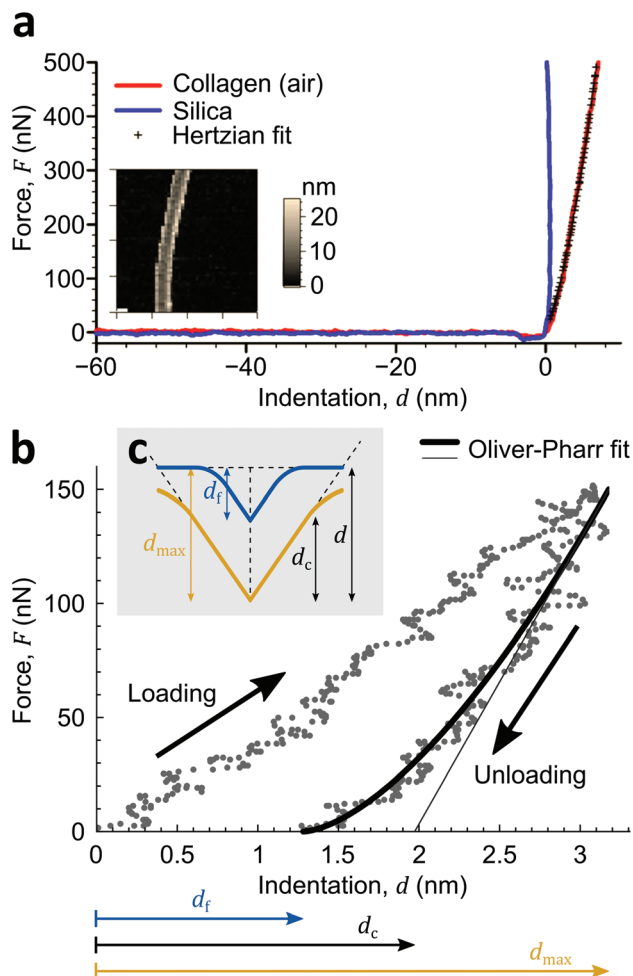
Fig. 4 (a) Force−indentation curves performed on a silica substrate (blue) and on the spine of a collagen fibril (red). The Hertz contact model of indentation ("+" markers) was fit to the collagen data. The force−volume plot is also shown (inset). Scan size: 2 μm. Adapted from ref. 107 with permission. (b) Force−indentation curve conducted on a collagen fibril, with both the loading and unloading curves shown. According to the Oliver−Pharr model,[108,109] a power law fit was performed on the unloading data (thick black line), while a line with slope $S = dF/dd$ was fit to the upper portion of the unloading data (thin black line). Adapted from ref. 110 with permission. (c) Oliver−Pharr model of a sample being deformed by an indenter,[108] with cross-sections of the sample in its maximally loaded (yellow, $d = d_{max}$) and final unloaded (blue, $d = d_f$) states. d_f: final indentation depth; d_c: contact indentation depth; d_{max}: maximum indentation.

confounding the model fit.[119] In several studies using Peak-Force QNM,[44,121–125] modulus values appear to have been sampled from the entire fibril width, not just from the spine. In some of these cases, variation in the modulus across the width of the fibril is apparent.[44,123,124] In other studies, however, little to no variation is seen along the diameter of the fibril,[44,121,122,125] likely because the tip diameter is of the same length scale as the fibril diameter—which introduces separate challenges, as discussed below. To what degree this practice of non-spine sampling misrepresents the true modulus remains to be directly studied.

Indentation depth

Indentation depth is crucial in any nanoindentation study of thin samples. Past studies on thin films established the "Bueckle rule", which states that indenting a sample to a depth of less than 10% of its thickness ($d/t < 0.1$) will probe the elastic modulus of the sample alone, not that of the substrate.[126–128] In agreement with these works, fibril indentation studies have displayed empirically consistent modulus results for $d/D < 0.1$ (Fig. 5).[44,110,123,124,129]

However, consistency may not imply accuracy: previous experiments and models of thin film indentation by Song and Pharr,[130,131] Hay and Crawford,[132] and others[133,134] have shown that the underlying substrate influences results even when $d/t < 0.1$, leading to a systematic overestimation of the modulus when the film is softer than the substrate. For example, according to Hay and Crawford's model, indenting a film whose stiffness is one tenth that of the underlying substrate results in a nearly 20% overestimation of the film modulus when $d/t = 0.08$.[132] These models have rarely been applied to fibril indentation studies,[44,135] perhaps because they describe a probe indenting a semi-infinite plane,[131–134] while small fibril indentation is best approximated by a sphere–cylinder geometry. Thus, there appears to be a need to apply the thin film models to the geometry of a fibril indentation scenario to account for substrate influence in the modulus results.

Further complications arise when indenting at extremely small (<5 nm) depths. If surface roughness is of the same length scale as indentation depth, the contact area function becomes unpredictable,[110,119,136] lateral deflection due to encountering asperities may affect the results,[119] and surface adhesion can have a significant impact on the contact area.[110] Indentation depths at the same scale as the surface roughness
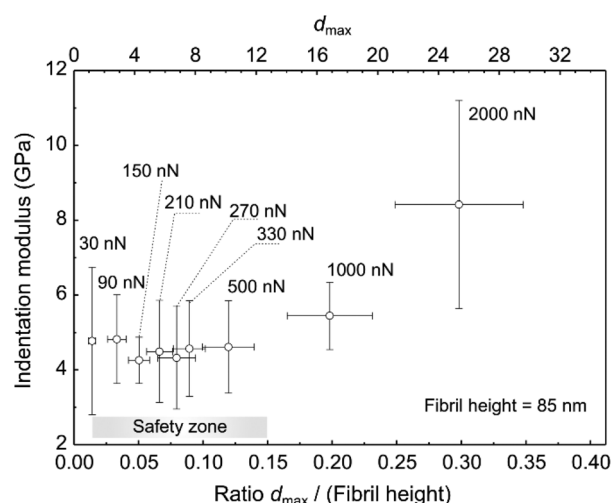

Fig. 5 Mean indentation modulus *versus* the maximum indentation depth to fibril ratio (lower *x*-axis) and *versus* the maximum indentation depth, d_{max} (upper *x*-axis) in nanoindentation testing of collagen fibrils. The applied load necessary to achieve each d_{max} is also given. Adapted from ref. 110 with permission.

therefore display a greater degree of variability and unreliability (see 30 nN data, Fig. 5), which led Wenger *et al.* to assign a 20% random error to their measurements in addition to the expected 20% AFM calibration error,[119] while other groups have simply discounted the returned moduli of asperities that are of the same length scale as the tip size.[110,118,136–139] These complications demand careful consideration of indentation depth for a given sample, and perhaps invite the need for further study of how to best characterize results at extremely small indentation depths.

Indentation model

Once all necessary test parameters and calibrations have been considered, the contact model used to fit the data has a significant impact on the final returned modulus.[96,110] If the diameter of the fibril is significantly larger than that of the tip (Fig. 3c), *e.g.* collagen fibrils (60–150 nm diameter) indented by a sharp tip (≈10 nm diameter), Wenger *et al.*[119,140] and Andriotis *et al.*[110] argued that the geometry can be approximated by a tip indenting a semi-infinite planar half-space. Since the authors employed indentation depths greater than the radius of the tip and observed plastic deformation of the fibril surface following testing, they employed Oliver–Pharr, the classic nanoindentation model that can accommodate an arbitrary tip shape and elastic-plastic deformation. Adhesion between the tip and sample is not accounted for in Oliver–Pharr, a shortcoming that has been argued to cause an overestimation of the modulus at small indentation depths in thin films, *i.e.* the "skin effect".[96,138,141] However, the skin effect appears to be mild or absent in fibril indentation studies,[110,129,135] perhaps due to the divergent stress field that results from a tip indenting a fibril[103] or differences in tip–substrate *vs.* tip–fibre adhesion.

Alternatively, the Hertz model of contact between two elastic spheres has been employed by Tan and Lim,[142] as well as many others,[107,129,143–147] in fibril indentation studies where $D_{fib} \gg D_{tip}$. Besides its inherent simplicity, the Hertz model has the advantage—*via* a straightforward variable transformation—of allowing the determination of the elastic modulus without knowledge of the zero contact point, which is notoriously difficult to pinpoint.[44,135,148] However, if the indentation depth exceeds the radius of the tip and plastic deformation occurs, the sphere–sphere and perfectly elastic contact assumptions of Hertz are an ill fit to the experimental conditions. For example, when Grant *et al.*[107] used the Hertz model, different modulus values were obtained if indentation marks were observed in the fibril following testing, implying that plastic deformation significantly affected the results. The authors addressed the issue by testing only at indentation depths that did not produce a mark,[107,144,145] but plastic deformation could be present and unobservable at the smaller depths.[107] Furthermore, as discussed above, indenting at extremely small depths introduces other confounding factors. Andriotis *et al.* applied both the Oliver–Pharr and Hertz models to the same force–indentation data and found a 34%

difference in the returned moduli, reflecting the importance of model choice in the ultimate result.[110]

When $D_{fib} \approx D_{tip}$ or $D_{fib} < D_{tip}$ (Fig. 3b), *e.g.* amyloid fibrils (<10 nm diameter) indented by even the sharpest probe, the geometry of contact departs dramatically from that of a probe indenting a flat surface, rendering Oliver–Pharr inapplicable. Guo *et al.*[135] and Sweers *et al.*[44] argued in their static nanoindentation studies of single amyloid fibrils that the Hertz sphere–sphere contact model is most appropriate in such scenarios, since the tip and fibril diameters are of the same length scale. The lack of hysteresis in the loading-unloading curve, plus the absence of an adhesive pull-off between tip and sample, further justified the use of the purely elastic Hertz model.[44,135] Similarly, the DMT model, which is based on the Hertz model yet includes a description of adhesion, is the standard model employed in PeakForce QNM studies of fibrils.[44,121,122,124,125] However, a sphere–plane geometry is standard in these PeakForce QNM works. Recently, an alternative model to the Hertz and DMT that describes a sphere–cylinder contact geometry was proposed: finite element analysis (FEA) was used to model the nanoindentation of a ≈100 nm diameter fibril with a ≈500 nm diameter probe.[103]

Regardless of the chosen model, indentation testing of small fibrils (when $D_{fib} \approx D_{tip}$ or $D_{fib} < D_{tip}$) requires the use of small indentation depths, which may introduce a host of confounding factors, as previously discussed. An additional, potentially crucial consideration is the force averaging that results when probing features smaller than the tip diameter.[149] If the target feature is small relative to the tip size, the adhesive force between the tip and underlying substrate is significant and has been explicitly observed in several fibril studies.[107,119,135] This tip–substrate adhesion will contribute to the net forces experienced by the tip while it indents the fibril,[149] resulting in a systematic underestimation of the modulus. Indeed, tip size was found to be inversely proportional to the returned modulus value, yielding a 70% decrease in the sample modulus when the tip radius was increased from 10 nm to 160 nm, but force averaging was not considered as an influencing factor.[44]

Other considerations

Besides the previous considerations, there may be other factors influencing nanoscale indentation experiments of fibrils. Most if not all fibrils are anisotropic by nature, so only the transverse elastic modulus—not the axial modulus—is accessible by nanoindentation. The yield strength may also be estimated by converting the nanoindentation data into a stress–strain curve,[101,150–152] but the shape of this resulting curve has been shown to only approximately match the shape of a stress–strain curve obtained from uniaxial tensile testing.[152] Additionally, an unknown in these and most other nanoscale mechanical tests is the Poisson's ratio of the material; the returned modulus is therefore the effective modulus, with the true modulus calculated from an estimate of the Poisson's ratio. Further calibrations may also be necessary to reduce error,[44,135] and the deflection sensitivity has been reported to

vary across a sample, requiring that the calibration procedure be conducted as close to the sample as possible.[135] Finally, the viscoelasticity of the sample is inaccessible *via* basic static or quasi-static techniques, but may still influence the results, especially when large forces are present.[14,153,154] The reader is referred to a recent review of dynamic nanoindentation techniques,[14] which are gaining in popularity and accessibility.

Conclusion

The advancing miniaturization of devices and progressing concentration of different functionalities within a material increasingly demand more sophisticated nanofibrillar building units. The characterization of these building units and the detailed examination of highly evolved natural systems that might serve as models for biomimicry both require high-resolution, reliable testing techniques to assess their respective mechanical spectra. The AFM provides a highly sensitive and thus highly attractive platform for this task. As reviewed here, the intense research conducted in the field of nanofibre mechanical testing in the past decades and the strong trend to implement mechanical mapping techniques in AFM instrumentations illustrate two key points. First, due to its simple sample preparation requirements and universal applicability, AFM-based mechanical fibre characterization is the method of choice for a vast majority of systems. Second, as indicated by the diversity of data interpretation efforts, AFM-based three-point deformation testing and indentation of nanoscale fibres are still not standardized to the degree of conventional macro-scale mechanical testing. However, with further efforts to disentangle the many challenges that are present at the nanoscale, the AFM's capabilities of nanoscale manipulation and *in situ* force-monitoring make it a uniquely powerful tool in the discovery of single fibre mechanics.

Acknowledgements

References

1 P. Fratzl and R. Weinkamer, *Prog. Mater. Sci.*, 2007, **52**, 1263–1334.
2 M. F. L. De Volder, S. H. Tawfick, R. H. Baughman and A. J. Hart, *Science*, 2013, **339**, 535–539.
3 A. Arinstein and E. Zussman, *J. Polym. Sci., Part B: Polym. Phys.*, 2011, **49**, 691–707.
4 A. S. Asran, V. Seydewitz and G. H. Michler, *J. Appl. Polym. Sci.*, 2012, **125**, 1663–1673.
5 C. Q. Sun, *Prog. Mater. Sci.*, 2009, **54**, 179–307.

6 X.-P. Zheng, Y.-P. Cao, B. Li, X.-Q. Feng and G.-F. Wang, *Nanotechnology*, 2010, **21**, 205702.
7 S. Y. Chew, T. C. Hufnagel, C. T. Lim and K. W. Leong, *Nanotechnology*, 2006, **17**, 3880.
8 V. V. Vasiliev and E. Morozov, *Advanced Mechanics of Composite Materials*, 3rd edn, 2013, vol. 3.
9 Y. Li, F. Qian, J. Xiang and C. M. Lieber, *Mater. Today*, 2006, **9**, 18–27.
10 A. Greiner and J. H. Wendorff, *Angew. Chem., Int. Ed.*, 2007, **46**, 5670–5703.
11 M. Heim, D. Keerl and T. Scheibel, *Angew. Chem., Int. Ed.*, 2009, **48**, 3584–3596.
12 T. J. Sill and H. A. von Recum, *Biomaterials*, 2008, **29**, 1989–2006.
13 S. Agarwal, A. Greiner and J. H. Wendorff, *Prog. Polym. Sci.*, 2013, **38**, 963–991.
14 S. R. Cohen and E. Kalfon-Cohen, *Beilstein J. Nanotechnol.*, 2013, **4**, 815–833.
15 Continuous Dynamic Analysis and Quasi-Static Measurement of Spider Silks, http://cp.literature.agilent.com/litweb/pdf/5990-4325EN.pdf (accessed March 2016).
16 Keysight T150 UTM Universal Testing Machine, http://literature.cdn.keysight.com/litweb/pdf/5990-4206EN.pdf (accessed March 2016).
17 B. Madsen, Z. Z. Shao and F. Vollrath, *Int. J. Biol. Macromol.*, 1999, **24**, 301–306.
18 B. Swanson, T. A. Blackledge, J. Beltrán and C. Hayashi, *Appl. Phys. A: Solid Surf.*, 2006, **82**, 213–218.
19 R. Work, *Text. Res. J.*, 1977, **47**, 650–662.
20 M. B. Bazbouz and G. K. Stylios, *J. Polym. Sci., Part B: Polym. Phys.*, 2010, **48**, 1719–1731.
21 T. D. Brown, A. Slotosch, L. Thibaudeau, A. Taubenberger, D. Loessner, C. Vaquette, P. D. Dalton and D. W. Hutmacher, *Biointerphases*, 2012, **7**, 13.
22 F. Chen, X. Peng, T. Li, S. Chen, X.-F. Wu, D. H. Reneker and H. Hou, *J. Phys. D: Appl. Phys.*, 2008, **41**, 025308.
23 R. Inai, M. Kotaki and S. Ramakrishna, *Nanotechnology*, 2005, **16**, 208.
24 S.-J. Park, G. G. Chase, K.-U. Jeong and H. Y. Kim, *J. Sol-Gel Sci. Technol.*, 2010, **54**, 188–194.
25 M.-F. Yu, O. Lourie, M. J. Dyer, K. Moloni, T. F. Kelly and R. S. Ruoff, *Science*, 2000, **287**, 637–640.
26 I. Kaplan-Ashiri, S. R. Cohen, K. Gartsman, R. Rosentsveig, G. Seifert and R. Tenne, *J. Mater. Res.*, 2004, **19**, 454–459.
27 P. E. Marszalek, W. J. Greenleaf, H. Li, A. F. Oberhauser and J. M. Fernandez, *Proc. Natl. Acad. Sci. U. S. A.*, 2000, **97**, 6282–6286.
28 G. Rubio-Bollinger, S. R. Bahn, N. Agraït, K. W. Jacobsen and S. Vieira, *Phys. Rev. Lett.*, 2001, **87**, 026101.
29 F. Hang, D. Lu, R. J. Bailey, I. Jimenez-Palomar, U. Stachewicz, B. Cortes-Ballesteros, M. Davies, M. Zech, C. Bödefeld and A. H. Barber, *Nanotechnology*, 2011, **22**, 365708.
30 E. P. S. Tan, C. N. Goh, C. H. Sow and C. T. Lim, *Appl. Phys. Lett.*, 2005, **86**, 073115.

31 E. P. S. Tan and C. T. Lim, *Rev. Sci. Instrum.*, 2004, **75**, 2581–2585.

32 J. S. Graham, A. N. Vomund, C. L. Phillips and M. Grandbois, *Exp. Cell Res.*, 2004, **299**, 335–342.

33 F. Hang and A. H. Barber, *J. R. Soc., Interface*, 2011, **8**, 500–505.

34 J. A. J. van der Rijt, K. O. van der Werf, M. L. Bennink, P. J. Dijkstra and J. Feijen, *Macromol. Biosci.*, 2006, **6**, 697–702.

35 R. B. Svensson, T. Hassenkam, P. Hansen and S. P. Magnusson, *J. Mech. Behav. Biomed. Mater.*, 2010, **3**, 112–115.

36 R. B. Svensson, H. Mulder, V. Kovanen and S. P. Magnusson, *Biophys. J.*, 2013, **104**, 2476–2484.

37 A. H. Barber, D. Lu and N. M. Pugno, *J. R. Soc., Interface*, 2015, **12**, 20141326.

38 P. Eaton and P. West, *Atomic force microscopy*, Oxford University Press, New York, 2010.

39 R. Proksch, T. E. Schaffer, J. P. Cleveland, R. C. Callahan and M. B. Viani, *Nanotechnology*, 2004, **15**, 1344–1350.

40 J. P. Cleveland, S. Manne, D. Bocek and P. K. Hansma, *Rev. Sci. Instrum.*, 1993, **64**, 403–405.

41 J. L. Hutter and J. Bechhoefer, *Rev. Sci. Instrum.*, 1993, **64**, 1868.

42 J. E. Sader, J. W. M. Chon and P. Mulvaney, *Rev. Sci. Instrum.*, 1999, **70**, 3967–3969.

43 Quantitative mechanical property mapping at the nanoscale with PeakForce QNM, https://www.bruker.com/fileadmin/user_upload/8-PDF-Docs/SurfaceAnalysis/AFM/ApplicationNotes/AN128-RevB0-Quantitative_Mechanical_Property_Mapping_at_the_Nanoscale_with_PeakForceQNM-AppNote.pdf (accessed March 2016).

44 K. Sweers, K. van der Werf, M. Bennink and V. Subramaniam, *Nanoscale Res. Lett.*, 2011, **6**, 270.

45 B. G. Demczyk, Y. M. Wang, J. Cumings, M. Hetman, W. Han, A. Zettl and R. O. Ritchie, *Mater. Sci. Eng., A*, 2002, **334**, 173–178.

46 S. Eppell, B. Smith, H. Kahn and R. Ballarini, *J. R. Soc., Interface*, 2006, **3**, 117–121.

47 M. A. Haque and M. T. A. Saif, *Exp. Mech.*, 2003, **43**, 248–255.

48 D. Jaeger, J. Schischka, J. Bagdahn and R. Jaeger, *J. Appl. Polym. Sci.*, 2009, **114**, 3774–3779.

49 M. Naraghi, I. Chasiotis, H. Kahn, Y. Wen and Y. Dzenis, *Rev. Sci. Instrum.*, 2007, **78**, 085108.

50 B. A. Samuel, M. A. Haque, B. Yi, R. Rajagopalan and H. C. Foley, *Nanotechnology*, 2007, **18**, 115704.

51 Y. Zhu and T.-H. Chang, *J. Micromech. Microeng.*, 2015, **25**, 093001.

52 Q. Guo, P. Landau, P. Hosemann, Y. Wang and J. R. Greer, *Small*, 2013, **9**, 691–696.

53 D. Magagnosc, R. Ehrbar, G. Kumar, M. He, J. Schroers and D. Gianola, *Sci. Rep.*, 2013, **3**, 1096.

54 T. W. Tombler, C. Zhou, L. Alexseyev, J. Kong, H. Dai, L. Liu, C. S. Jayanthi, M. Tang and S.-Y. Wu, *Nature*, 2000, **405**, 769–772.

55 J.-P. Salvetat, G. A. D. Briggs, J.-M. Bonard, R. R. Bacsa, A. J. Kulik, T. Stöckli, N. A. Burnham and L. Forró, *Phys. Rev. Lett.*, 1999, **82**, 944–947.

56 B. Wu, A. Heidelberg and J. J. Boland, *Nat. Mater.*, 2005, **4**, 525–529.

57 C. R. Carlisle, C. Coulais, M. Namboothiry, D. L. Carroll, R. R. Hantgan and M. Guthold, *Biomaterials*, 2009, **30**, 1205–1213.

58 D. Almecija, D. Blond, J. E. Sader, J. N. Coleman and J. J. Boland, *Carbon*, 2009, **47**, 2253–2258.

59 W. Liu, L. M. Jawerth, E. A. Sparks, M. R. Falvo, R. R. Hantgan, R. Superfine, S. T. Lord and M. Guthold, *Science*, 2006, **313**, 634–634.

60 L. Yang, C. F. C. Fitié, K. O. van der Werf, M. L. Bennink, P. J. Dijkstra and J. Feijen, *Biomaterials*, 2008, **29**, 955–962.

61 L. Yang, K. O. van der Werf, C. F. C. Fitié, M. L. Bennink, P. J. Dijkstra and J. Feijen, *Biophys. J.*, 2008, **94**, 2204–2211.

62 W. Wang and A. H. Barber, *J. Polym. Sci., Part B: Polym. Phys.*, 2012, **50**, 546–551.

63 A. Gestos, P. G. Whitten, G. G. Wallace and G. M. Spinks, *Soft Matter*, 2012, **8**, 8082–8087.

64 E. K. McCarthy, A. T. Bellew, J. E. Sader and J. J. Boland, *Nat. Commun.*, 2014, **5**, 4336.

65 E. D. Minot, Y. Yaish, V. Sazonova, J. Y. Park, M. Brink and P. L. McEuen, *Phys. Rev. Lett.*, 2003, **90**, 156401.

66 A. Heidelberg, L. T. Ngo, B. Wu, M. A. Phillips, S. Sharma, T. I. Kamins, J. E. Sader and J. J. Boland, *Nano Lett.*, 2006, **6**, 1101–1106.

67 Y. Calahorra, O. Shtempluck, V. Kotchetkov and Y. E. Yaish, *Nano Lett.*, 2015, **15**, 2945–2950.

68 D. Kluge, J. C. Singer, J. W. Neubauer, F. Abraham, H. W. Schmidt and A. Fery, *Small*, 2012, **8**, 2563–2570.

69 C. P. Green, H. Lioe, J. P. Cleveland, R. Proksch, P. Mulvaney and J. E. Sader, *Rev. Sci. Instrum.*, 2004, **75**, 1988–1996.

70 M. Munz, *J. Phys. D: Appl. Phys.*, 2010, **43**, 063001.

71 J. M. Gere and S. P. Timoshenko, in *Mechanics of Materials*, Chapman & Hall, London, 3rd edn, 1991, p. 692.

72 D. Kluge, F. Abraham, S. Schmidt, H.-W. Schmidt and A. Fery, *Langmuir*, 2010, **26**, 3020–3023.

73 D. Kluge, J. C. Singer, B. R. Neugirg, J. W. Neubauer, H. W. Schmidt and A. Fery, *Polymer*, 2012, **53**, 5754–5759.

74 A. E. Tanur, J. Wang, A. L. M. Reddy, D. N. Lamont, Y. K. Yap and G. C. Walker, *J. Phys. Chem. B*, 2013, **117**, 4618–4625.

75 Y. X. Chen, B. L. Dorgan, D. N. McIlroy and D. E. Aston, *J. Appl. Phys.*, 2006, **100**, 104301.

76 M. Cronin-Golomb and O. Sahin, *Beilstein J. Nanotechnol.*, 2013, **4**, 243–248.

77 X. Y. Ling, I. Y. Phang, H. Schonherr, D. N. Reinhoudt, G. J. Vancso and J. Huskens, *Small*, 2009, **5**, 1428–1435.

78 Y. X. Chen, I. Stevenson, R. Pouy, L. D. Wang, D. N. McIlroy, T. Pounds, M. G. Norton and D. E. Aston, *Nanotechnology*, 2007, **18**, 135708.

79 S. Iwamoto, W. Kai, A. Isogai and T. Iwata, *Biomacromolecules*, 2009, **10**, 2571–2576.

80 U. Stachewicz, R. J. Bailey, W. Wang and A. H. Barber, *Polymer*, 2012, **53**, 5132–5137.

81 X. Y. Tao, L. X. Dong, X. N. Wang, W. K. Zhang, B. J. Nelson and X. D. Li, *Adv. Mater.*, 2010, **22**, 2055–2059.

82 S. D. Hudson, V. Zhurov, V. Grbic, M. Grbic and J. L. Hutter, *J. Appl. Phys.*, 2013, **113**, 154307.

83 Q. Xiong, N. Duarte, S. Tadigadapa and P. C. Eklund, *Nano Lett.*, 2006, **6**, 1904–1909.

84 E. Celik, I. Guven and E. Madenci, *Nanotechnology*, 2011, **22**, 155702.

85 L. T. Ngo, D. Almecija, J. E. Sader, B. Daly, N. Petkov, J. D. Holmes, D. Erts and J. J. Boland, *Nano Lett.*, 2006, **6**, 2964–2968.

86 B. M. Wen, J. E. Sader and J. J. Boland, *Phys. Rev. Lett.*, 2008, **101**, 175502.

87 B. Wu, A. Heidelberg, J. J. Boland, J. E. Sader, X. M. Sun and Y. D. Li, *Nano Lett.*, 2006, **6**, 468–472.

88 Y. E. Yaish, Y. Calahorra, O. Shtempluck and V. Kotchetkov, *J. Appl. Phys.*, 2015, **117**, 2945–2950.

89 H. C. Schniepp, S. R. Koebley and F. Vollrath, *Adv. Mater.*, 2013, **25**, 7028–7032.

90 A. Gestos, P. G. Whitten, G. M. Spinks and G. G. Wallace, *Polym. Test.*, 2013, **32**, 655–664.

91 W. Liu, C. R. Carlisle, E. A. Sparks and M. Guthold, *J. Thromb. Haemostasis*, 2010, **8**, 1030–1036.

92 C. R. Carlisle, C. Coulais and M. Guthold, *Acta Biomater.*, 2010, **6**, 2997–3003.

93 D. M. Ebenstein and L. A. Pruitt, *Nano Today*, 2006, **1**, 26–33.

94 M. R. VanLandingham, *J. Res. Nat. Inst. Stand. Technol.*, 2003, **108**, 249–265.

95 A. M. Díez-Pascual, M. A. Gómez-Fatou, F. Ania and A. Flores, *Prog. Mater. Sci.*, 2015, **67**, 1–94.

96 M. E. Dokukin and I. Sokolov, *Macromolecules*, 2012, **45**, 4277–4288.

97 The MFP Instrumented NanoIndenter for Quantitative Materials Characterization, https://www.asylumresearch.com/Products/NanoIndenter/NanoIndentDSHR.pdf (accessed March 2016).

98 NanoForce Nanomechanical Testing System, https://www.bruker.com/fileadmin/user_upload/8-PDF-Docs/Surface-Analysis/TMT/Brochures/B1003-RevB0_NanoForce_Nano-mechanical_Testing-Brochure.pdf (accessed March 2016).

99 X. Li, H. Gao, C. J. Murphy and K. K. Caswell, *Nano Lett.*, 2003, **3**, 1495–1498.

100 X. Li, X. Wang, Q. Xiong and P. C. Eklund, *Nano Lett.*, 2005, **5**, 1982–1986.

101 M. Lucas, A. M. Leach, M. T. McDowell, S. E. Hunyadi, K. Gall, C. J. Murphy and E. Riedo, *Phys. Rev. B: Condens. Matter*, 2008, **77**, 245420.

102 X. Tao, X. Wang and X. Li, *Nano Lett.*, 2007, **7**, 3172–3176.

103 M. Zeeshan, D. Esqué-de Los Ojos, P. Castro-Hartmann, M. Guerrero, J. Nogués, S. Suriñach, M. Baró, B. Nelson, S. Pané, E. Pellicer and J. Sort, *Nanoscale*, 2016, **8**, 1344–1351.

104 D. J. Müller and Y. F. Dufrêne, *Nat. Nanotechnol.*, 2008, **3**, 261–269.

105 D. J. Müller and Y. F. Dufrêne, *Trends Cell Biol.*, 2011, **21**, 461–469.

106 E. P. S. Tan and C. T. Lim, *Compos. Sci. Technol.*, 2006, **66**, 1102–1111.

107 C. A. Grant, D. J. Brockwell, S. E. Radford and N. H. Thomson, *Appl. Phys. Lett.*, 2008, **92**, 233902.

108 W. C. Oliver and G. M. Pharr, *J. Mater. Res.*, 2004, **19**, 3–20.

109 W. C. Oliver and G. M. Pharr, *J. Mater. Res.*, 1992, **7**, 1564–1583.

110 O. G. Andriotis, W. Manuyakorn, J. Zekonyte, O. L. Katsamenis, S. Fabri, P. H. Howarth, D. E. Davies and P. J. Thurner, *J. Mech. Behav. Biomed. Mater.*, 2014, **39**, 9–26.

111 H. Hertz, *J. Reine Angew. Math.*, 1882, **94**, 156–171.

112 J. Israelachvili, *Intermolecular and surface forces*, 2nd edn, 1998.

113 K. L. Johnson and K. L. Johnson, *Contact mechanics*, Cambridge University Press, 1987.

114 M. R. VanLandingham, J. S. Villarrubia and G. Meyers, in *Proceedings of the SEM IX International Congress on Experimental Mechanics*, Society for Engineering Mechanics, Inc, 2000, pp. 912–915.

115 J. Adamcik and R. Mezzenga, *Curr. Opin. Colloid Interface Sci.*, 2012, **17**, 369–376.

116 Expanding Atomic Force Microscopy with HybriD Mode Imaging, http://www.ntmdt.com/data/media/files/resources/special-applications/hybrid-mode/Expanding_Atomic_Force_Microscopy_with_Hybrid_Mode_Imaging_AN087.pdf (accessed March 2016).

117 The NanomechPro Toolkit, https://www.asylumresearch.com/Products/NanomechPro/NanomechPro-Toolkit-AFM.pdf (accessed March 2016).

118 M. Stolz, R. Raiteri, A. U. Daniels, M. R. VanLandingham, W. Baschong and U. Aebi, *Biophys. J.*, 2004, **86**, 3269–3283.

119 M. P. E. Wenger, L. Bozec, M. A. Horton and P. Mesquida, *Biophys. J.*, 2007, **93**, 1255–1263.

120 Applications of Force Volume Imaging with Atomic Force Microscopes, http://nano.boisestate.edu/wp-content/uploads/2010/12/Bruker-AN-20-Force-Volume-Spectroscopy.pdf (accessed March 2016).

121 J. Adamcik, A. Berquand and R. Mezzenga, *Appl. Phys. Lett.*, 2011, **98**, 193701.

122 J. Adamcik, C. Lara, I. Usov, J. S. Jeong, F. S. Ruggeri, G. Dietler, H. A. Lashuel, I. W. Hamley and R. Mezzenga, *Nanoscale*, 2012, **4**, 4426.

123 G. Lamour, C. K. Yip, H. Li and J. Gsponer, *ACS Nano*, 2014, **8**, 3851–3861.

124 F. S. Ruggeri, J. Adamcik, J. S. Jeong, H. A. Lashuel, R. Mezzenga and G. Dietler, *Angew. Chem., Int. Ed.*, 2015, **54**, 2462–2466.

125 K. K. M. Sweers, K. O. van der Werf, M. L. Bennink and V. Subramaniam, *ACS Nano*, 2012, **6**, 5952–5960.

126 H. Bueckle, in *The Science of Hardness Testing and Its Applications*, ed. H. Westbrook and H. Conrad, 1973, pp. 453–491.

127 K. Geng, F. Yang, T. Druffel and E. A. Grulke, *Polymer*, 2005, **46**, 11768–11772.

128 K. Miyake, N. Satomi and S. Sasaki, *Appl. Phys. Lett.*, 2006, **89**, 031925.

129 A. J. Heim, W. G. Matthews and T. J. Koob, *Appl. Phys. Lett.*, 2006, **89**, 181902.

130 H. Song, *PhD thesis*, Rice University, 1999.

131 H. Xu and G. M. Pharr, *Scr. Mater.*, 2006, **55**, 315–318.

132 J. Hay and B. Crawford, *J. Mater. Res.*, 2011, **26**, 727–738.

133 B. B. Akhremitchev and G. C. Walker, *Langmuir*, 1999, **15**, 5630–5634.

134 C. A. Clifford and M. P. Seah, *Nanotechnology*, 2006, **17**, 5283–5292.

135 S. Guo and B. B. Akhremitchev, *Biomacromolecules*, 2006, **7**, 1630–1636.

136 A. C. Fischer-Cripps, *Factors Affecting Nanoindentation Test Data*, Springer, 2000.

137 M. I. Dafinone, G. Feng, T. Brugarolas, K. E. Tettey and D. Lee, *ACS Nano*, 2011, **5**, 5078–5087.

138 M. E. Dokukin and I. Sokolov, *Langmuir*, 2012, **28**, 16060–16071.

139 C. Walter and C. Mitterer, *Surf. Coat. Technol.*, 2009, **203**, 3286–3290.

140 M. P. E. Wenger, M. A. Horton and P. Mesquida, *Nanotechnology*, 2008, **19**, 384006.

141 M. E. Dokukin, N. V. Guz and I. Sokolov, *Biophys. J.*, 2013, **104**, 2123–2131.

142 E. P. S. Tan and C. T. Lim, *Appl. Phys. Lett.*, 2005, **87**, 123106.

143 B. W. Ahn and T. J. Kang, *J. Appl. Polym. Sci.*, 2012, **125**, 1567–1575.

144 C. A. Grant, D. J. Brockwell, S. E. Radford and N. H. Thomson, *Biophys. J.*, 2009, **97**, 2985–2992.

145 C. A. Grant, M. A. Phillips and N. H. Thomson, *J. Mech. Behav. Biomed. Mater.*, 2012, **5**, 165–170.

146 M. Minary-Jolandan and M.-F. Yu, *Biomacromolecules*, 2009, **10**, 2565–2570.

147 R. M. A. Sullan, N. Gunari, A. E. Tanur, Y. Chan, G. H. Dickinson, B. Orihuela, D. Rittschof and G. C. Walker, *Biofouling*, 2009, **25**, 263–275.

148 E. M. Darling, *Nanotechnology*, 2011, **22**, 175707.

149 S. Santos, V. Barcons, H. K. Christenson, J. Font and N. H. Thomson, *PLoS One*, 2011, **6**, e23821.

150 S. Basu, A. Moseson and M. W. Barsoum, *J. Mater. Res.*, 2006, **21**, 2628–2637.

151 J. Field and M. Swain, *J. Mater. Res.*, 1995, **10**, 101–112.

152 E. Herbert, G. Pharr, W. Oliver, B. Lucas and J. Hay, *Thin Solid Films*, 2001, **398**, 331–335.

153 D. Tranchida, Z. Kiflie, S. Acierno and S. Piccarolo, *Meas. Sci. Technol.*, 2009, **20**, 095702.

154 D. Tranchida, Z. Kiflie and S. Piccarolo, *Macromolecules*, 2007, **40**, 7366–7371.